



# EXAFS and kinetic study of $\text{MnO}_x/\gamma\text{-alumina}$ in gas phase catalytic oxidation of toluene by ozone

Ebrahim Rezaei, Jafar Soltan\*

Department of Chemical and Biological Engineering, University of Saskatchewan, 57 Campus Drive, Saskatoon S7N 5A9, SK, Canada

## ARTICLE INFO

### Article history:

Received 3 July 2013

Received in revised form

17 September 2013

Accepted 19 October 2013

Available online 28 October 2013

### Keywords:

Toluene

Ozone

Manganese oxides

EXAFS

Kinetic study

## ABSTRACT

This work addresses characterization of  $\text{Mn}_2\text{O}_3$  materials by EXAFS technique and the mechanism of toluene oxidation by ozone over  $\text{MnO}_x/\gamma\text{-alumina}$  (10%) catalyst. Bond Valence Model was used to model EXAFS signal of bulk and nano-particles of  $\text{Mn}_2\text{O}_3$ . The Bond Valence Model relates formal oxidation state of Mn atoms to the coordination number of oxygen atoms at the first Mn shell, adding restraints to the EXAFS theoretical models. Use of the Bond Valence Model resulted in distinguishing closely located oxygen atoms around each Mn site without any simplifying assumption on the structure of  $\text{Mn}_2\text{O}_3$ . Kinetic study of catalytic oxidation of toluene by ozone using  $\text{MnO}_x/\gamma\text{-alumina}$  (10%) was performed at constant toluene or ozone partial pressures by varying the reactor space time in the range of 0–1212  $\text{kg}_{\text{cat.}} \text{mol}_{\text{tol.}}^{-1} \text{s}$ . Differential method of analysis was used to estimate the initial reaction rates. Apparent activation energy of the reaction was determined to be 31  $\text{kJ mol}^{-1}$ , obtained by a power law model. The power law model also determined the reaction orders with respect to toluene and ozone as –1 and 2, respectively. To explain the initial reaction rates, two Langmuir–Hinshelwood mechanisms based on different toluene activation steps were examined. The first mechanism was based on activation of adsorbed toluene molecule by atomic oxygen while the second model was based on activation of toluene molecule via abstraction of hydrogen from the methyl group. The second Langmuir–Hinshelwood mechanism led to the same rate equation as the power law model, explaining the effect of toluene and ozone partial pressures on toluene oxidation rate.

© 2013 Elsevier B.V. All rights reserved.

## 1. Introduction

There has been increasing concern over indoor and outdoor air quality in recent years due to public and environmental health and safety issues. People are now dealing with the problem of air pollution more than the past because of living in metropolitan areas and spending their time in enclosed environments. This has led to development of air purification technologies based on sorption filtration, combustion processes and photo-catalytic oxidation to remove pollutants from air or convert them into less harmful by-products.

Catalytic ozonation is an innovative method for oxidation of pollutants in liquid or gas phase [1]. Application of this method in gas phase has opened a new catalytic approach for low temperature oxidation of volatile organic compounds (VOCs) at trace concentration levels. Ethanol, carbon monoxide, acetone, cyclohexane, benzene, chlorobenzene, toluene and formaldehyde are among the pollutants which were oxidized by ozone over various catalysts [2–11]. Results show that apparent activation energy of VOCs

oxidation can be greatly reduced by use of ozone compared to that of oxygen, making total oxidation of VOCs possible at temperatures as low as 100 °C or even lower.

Manganese oxides ( $\text{MnO}_x$ ) are among the most active transition metal oxides for low temperature decomposition of ozone to generate active oxygen species required for oxidation of VOCs [12]. It is believed that the exceptional catalytic activity of  $\text{MnO}_x$  is related to the capability of these oxides to have different oxidation states during a catalytic cycle, making this catalyst suitable for oxidation of VOCs by ozone [13]. Even though the effectiveness of catalytic ozonation of VOCs over  $\text{MnO}_x$  has been accepted widely, there are still unclear issues in the literature which need to be addressed.

Although the presence of  $\text{Mn}_3\text{O}_4$ ,  $\text{Mn}_2\text{O}_3$  and  $\text{MnO}_2$  are frequently reported in supported manganese oxide catalysts [10,13,14], there are a few studies on atomic structure of manganese oxides performed by extended X-ray absorption fine structure (EXAFS) [13,15–18]. The EXAFS study of  $\text{MnO}_2$  is fairly straightforward since it has only one Mn site. But difficulty arises in EXAFS analysis of  $\text{Mn}_2\text{O}_3$  and  $\text{Mn}_3\text{O}_4$  due to the existence of two Mn sites and several sets of oxygen atoms located closely at the first shell around the Mn sites. These oxygen atoms are separated by approximately 0.1–0.3 Å, making it difficult for them to be distinguished by the sole EXAFS fitting procedure. Usually the

\* Corresponding author. Tel.: +1 306 966 5449; fax: +1 306 966 4777.

E-mail address: [j.soltan@usask.ca](mailto:j.soltan@usask.ca) (J. Soltan).

## Nomenclature

CN	coordination number (-)
$d_p$	particle size ( $\mu\text{m}$ )
$E$	activation energy ( $\text{kJ mol}^{-1}$ )
$\Delta E_0$	difference between theory and data in EXAFS energy scale (eV)
$F_c$	$F$ value in Fisher's $F$ -test
$F_{\text{tol.}}$	toluene molar flow rate ( $\text{mol}_{\text{tol.}} \text{s}^{-1}$ )
$\Delta H$	enthalpy of adsorption ( $\text{kJ mol}^{-1}$ )
$k$	kinetic rate constant ( $\text{atm}^{-1}$ , $\text{mol}_{\text{tol.}} \text{kg}_{\text{cat.}}^{-1} \text{s}^{-1} \text{atm}^{-2}$ or $\text{mol}_{\text{tol.}} \text{kg}_{\text{cat.}}^{-1} \text{s}^{-1} \text{atm}^{-1}$ )
$k_0$	pre-exponential factor of kinetic rate constant ( $\text{atm}^{-1}$ , $\text{mol}_{\text{tol.}} \text{kg}_{\text{cat.}}^{-1} \text{s}^{-1} \text{atm}^{-2}$ or $\text{mol}_{\text{tol.}} \text{kg}_{\text{cat.}}^{-1} \text{s}^{-1} \text{atm}^{-1}$ )
$K$	equilibrium constant (-)
$K_{\text{tol.}}$	toluene pressure equilibrium constant ( $\text{atm}^{-1}$ )
Mn1	first Mn site in $\text{Mn}_2\text{O}_3$ structure
Mn2	second Mn site in $\text{Mn}_2\text{O}_3$ structure
$p$	number of fitting parameter (-)
$P$	pressure (atm)
$r$	reaction rate ( $\text{mol}_{\text{tol.}} \text{kg}_{\text{cat.}}^{-1} \text{s}^{-1}$ )
$R_f$	absolute misfit between theory and data in EXAFS fitting (-)
$R_o'$	empirical parameter in the bond valence definition
$R_{ij}$	interatomic distance between cation $i$ and anion $j$ (Å)
$\Delta R$	change in the bond length between atoms (Å)
$S$	selectivity (-)
$S_0^2$	amplitude reduction factor (-)
$S_{ij}$	valence of the bond between cation $i$ and anion $j$ (-)
$\Delta S$	entropy of adsorption ( $\text{J mol}^{-1} \text{K}^{-1}$ )
$T$	temperature ( $^\circ\text{C}$ or K)
$V_i$	formal oxidation state of cation $i$ (-)
$W_{\text{cat.}}$	catalyst weight (kg)
$X_{\text{tol.}}$	toluene conversion ( $\text{mol}_{\text{tol.}} \text{mol}_{\text{tol,in}}^{-1}$ )
<i>Greek letters</i>	
$\theta$	fraction of occupied or vacant catalyst active sites
$v$	theoretical stoichiometric coefficient
$\sigma^2$	mean-square displacement of the bond length ( $\text{\AA}^2$ )
$\chi^2_v$	reduced chi-square
<i>Subscripts</i>	
cal.	calculated
cat.	catalyst
eff.	effective
exp.	experimental
in	inlet
O	oxygen
oz.	ozone
tol.	toluene
<i>Superscripts</i>	
app.	apparent
o	standard state of gases
*	catalyst active site

two sites are integrated into a single site to reduce the complexity of the problem and to fit the EXAFS signal [10,13]. The method has shown to be acceptable, even though no attempt has yet been made to resolve this problem with a more general approach to show the validity of the averaging method.

Another issue which is still not completely clear is the mechanism of catalytic ozonation of aromatic molecules such as benzene and toluene by ozone and relevant kinetic steps involved in the mechanism. Reed et al. have studied catalytic oxidation of acetone by ozone over silica supported manganese oxides using in-situ Raman spectroscopy [19]. They have concluded that the oxidation reaction occurs on the surface of the catalyst between atomic oxygen and adsorbed acetone molecule, leading to a Langmuir–Hinshelwood type of mechanism. However, the proposed mechanism and the related kinetic equations have not yet been tested on VOCs other than acetone to explore the generality of this mechanism. It is also a matter of uncertainty how different VOCs are activated on the catalyst active sites and how many active sites are required for their activation.

This paper presents the results of our work to fit the EXAFS signal of  $\text{Mn}_2\text{O}_3$  materials without combining the two Mn sites by using Bond Valence Model. The Bond Valence Model correlates oxidation state of the Mn atoms to coordination number of the oxygen atoms. This model essentially adds constraints or restraints on EXAFS fitting, allowing the closely located oxygen atoms in the structure of  $\text{Mn}_2\text{O}_3$  to be distinguished. The paper also investigates the possible elementary steps involved in the catalytic oxidation of toluene by ozone over alumina supported manganese oxides catalysts. This was carried out by analysis of the effect of toluene and ozone partial pressures on the initial reaction rate and testing the applicability of the available elementary steps reported in the literature to the catalytic ozonation of toluene [19]. The paper also proposes possible alternative elementary steps which can better explain the observed kinetic data of catalytic toluene oxidation by ozone.

## 2. Experimental and data analysis

### 2.1. Synthesis and characterization of $\text{MnO}_x/\gamma$ -alumina (10%)

$\gamma$ -Alumina (Alfa Aesar,  $S_{\text{BET}} = 220 \text{ m}^2/\text{g}$ ) was impregnated by aqueous solution of manganese (II) nitrate tetrahydrate (Sigma–Aldrich, 97%) to synthesize  $\text{MnO}_x/\gamma$ -alumina with Mn loading of 10%. The impregnated support was dried at  $100^\circ\text{C}$  for 10 h and calcined in furnace under atmospheric air at  $500^\circ\text{C}$  for 4 h. The final catalyst was crushed and sieved to obtain particle size distribution in the range of 0–417  $\mu\text{m}$ . Bulk  $\text{Mn}_2\text{O}_3$  (Sigma–Aldrich, 99%, bixbyite phase) was used as the reference material in the EXAFS studies.

Characterization of  $\text{MnO}_x/\gamma$ -alumina (10%) has been previously carried out by our research group using inductively coupled plasma mass spectrometry (ICP-MS), X-ray diffraction (XRD), laser Raman spectroscopy, hydrogen temperature programmed reduction ( $\text{H}_2$ -TPR), X-ray absorption near edge structure (XANES) and extended X-ray absorption fine structure (EXAFS) techniques [10,20,21]. ICP-MS determined the actual loading of Mn to be 9.84% which was very close to the design value at 10%. The results of XRD, laser Raman spectroscopy and  $\text{H}_2$ -TPR indicated that two phases of manganese oxides,  $\text{MnO}_2$  (pyrolusite) and  $\text{Mn}_2\text{O}_3$  (bixbyite), were formed on the catalyst surface. XANES analysis showed that absorption energy of Mn  $K$ -edge of the catalyst (6548.4 eV) was close to that of  $\text{Mn}_2\text{O}_3$  (6548.1 eV) reference material, suggesting that formal Mn oxidation state was close to +3. Linear combination fitting of the XANES spectra of the catalyst with  $\text{MnO}_2$  and  $\text{Mn}_2\text{O}_3$  reference materials showed that the percentage of  $\text{Mn}_2\text{O}_3$  and  $\text{MnO}_2$  in the catalyst was 91.0 and 9.0%, respectively. Fourier transform (FT) of the EXAFS signal of the catalyst also confirmed that  $\text{Mn}_2\text{O}_3$  was the most abundant phase of manganese oxides in the catalyst which is considered as the catalyst active site in this work.

## 2.2. EXAFS data modeling and analysis

EXAFS data of Mn *K*-edge were obtained at Hard X-ray Micro-Analysis (HXMA) beamline at Canadian Light Source (CLS) [10,22]. The samples were diluted with boron nitride to result in approximately one unit edge jump at Mn *K*-edge. Scan step-size of the EXAFS region was set at  $0.05\text{ \AA}^{-1}$ . Athena software was used for energy calibration, background removal, averaging and normalization of the data [23]. Theoretical EXAFS models of  $\text{Mn}_2\text{O}_3$  reference material and  $\text{MnO}_x/\gamma$ -alumina (10%) were constructed and fitted to the experimental data in Artemis [24,25]. The fitting parameters of the reference material ( $\text{Mn}_2\text{O}_3$ ) were amplitude reduction factor ( $S_o^2$ ), bond length change between atoms ( $\Delta R$ ), change in energy scale between data and theory ( $\Delta E_0$ ) and mean-square displacement of the bond length ( $\sigma^2$ ) while the coordination numbers (CNs) were fixed from crystallography data of  $\text{Mn}_2\text{O}_3$ . The obtained amplitude reduction factor from the reference material was used as a fixed parameter in EXAFS fitting of  $\text{MnO}_x/\gamma$ -alumina (10%) to estimate CNs,  $\Delta R$ ,  $\Delta E_0$  and  $\sigma^2$  of the catalyst. EXAFS fitting were carried out with *k*-weight of 1 for the  $\text{Mn}_2\text{O}_3$  reference material and the catalyst. Sine window function with  $\Delta k$  of  $1\text{ \AA}^{-1}$  was used and the Fourier transforms were conducted in  $3\text{--}13\text{ \AA}^{-1}$  range. EXAFS fittings were performed in R space from 1 to  $3.7\text{ \AA}$ .

In order to construct a robust model for fitting of the data, the Bond Valence Model was used in the modeling of the EXAFS data which is based on Pauling's 2nd rule of electrostatic valence [26]. According to this model, formal oxidation state of the cation *i* is equal to the sum of valence of the bond between the cation and surrounding anions *j*:

$$V_i = \sum_j s_{ij} \quad (1)$$

in which, the bond valence ( $s_{ij}$ ) is defined by:

$$s_{ij} = \exp \left[ \frac{(R'_o - R_{ij})}{b} \right] \quad (2)$$

$R'_o$  and  $b$  are empirical parameters and  $R_{ij}$  is interatomic distance between the cation *i* and the anion *j* which can be coupled to EXAFS models. It has been shown that  $b$  has a universal value of 0.37 [26]. If there is only one type of anions around the cation,  $R_{ij}$  can be extracted from Eq. (2) and expressed as:

$$R_{ij} = R'_o + 0.37 \ln \left( \frac{\text{CN}_{ij}}{V_i} \right) \quad (3)$$

where  $\text{CN}_{ij}$  is the coordination number of the anion *j* around the cation *i* at distance  $R_{ij}$ . Eq. (3) correlates the interatomic bond length to the coordination number of the anions and oxidation state of the cation. This allows using a prior knowledge of the cation oxidation state, available from XANES analysis, in the EXAFS fitting which results in reduction of the number of fitting parameters. Even though it is possible to directly use Eq. (3) in the EXAFS analysis to remove  $\Delta R$  or CN from the fitting parameters, it is recommended to use Eq. (1) as a restraint to model EXFAS signals [26]. The reason relies on inaccuracy of Eqs. (1) and (2) leading to unreliable fitting parameters in EXAFS when their exact definitions are used as constraints. Therefore, it is decided to use the Bond Valence Model as a restraint in the EXAFS fitting of  $\text{Mn}_2\text{O}_3$  which adds a penalty term on EXAFS minimization objective function to keep the oxidation state of Mn ions close to their formal valence obtained from XANES analysis which is +3.

$\text{Mn}_2\text{O}_3$  has two Mn sites with occupancy of 25 and 75% [10]. The first site (Mn1) is surrounded by 6 oxygen atoms at  $1.993\text{ \AA}$  whereas three sets of two oxygen atoms are found around the second site (Mn2) at  $1.899$ ,  $1.985$  and  $2.248\text{ \AA}$ . Spatial structure of the two Mn sites and their surrounding oxygen atoms is presented in Fig. S.1 of

the Supplementary document. Considering the value of  $R_o'$  for the two Mn sites in  $\text{Mn}_2\text{O}_3$  (1.760 [27]), application of Eqs. (1) and (2) results in the following equations for the two Mn sites:

$$V_{\text{Mn}1} = \text{CN}_0 \exp \left[ \frac{(1.76 - R_{0,\text{site } 1})}{0.37} \right] \quad (4)$$

$$\begin{aligned} V_{\text{Mn}2} = & \left( \frac{\text{CN}_0}{3} \right) \exp \left[ \frac{(1.76 - R_{01,\text{site } 2})}{0.37} \right] \\ & + \left( \frac{\text{CN}_0}{3} \right) \exp \left[ \frac{(1.76 - R_{0,\text{site } 1})}{0.37} \right] \\ & + \left( \frac{\text{CN}_0}{3} \right) \exp \left[ \frac{(1.76 - R_{02,\text{site } 2})}{0.37} \right] \end{aligned} \quad (5)$$

where  $\text{CN}_0$  represents the total number of oxygen atoms at the first shell of  $\text{Mn}_2\text{O}_3$  materials which can be set at 6 for the reference material or obtained from EXAFS fitting of the catalysts.  $R_{0,\text{site } 1}$  is used to represent the interatomic distance of the oxygen atoms at  $1.993$  and  $1.985\text{ \AA}$  in the first and second Mn sites, respectively. The distances of the other two oxygen atoms at  $1.899$  and  $2.248\text{ \AA}$  in site 2 were denoted by  $R_{01,\text{site } 2}$  and  $R_{02,\text{site } 2}$ , respectively. Eqs. (4) and (5) were defined as restraints in Artemis and their values were restricted between 0 and 3 with a moderate penalty coefficient. It has to be noted that amplitude reduction factors were multiplied by Mn site occupancies in order to consider paths in each Mn sites. Goodness of EXAFS fittings were evaluated in terms of percentage of absolute misfit between theory and data ( $R_f$ ) and reduced chi-square ( $\chi_v^2$ ) [28]. It is recommended that fittings with lower  $R_f$  and  $\chi_v^2$  have higher statistical significance.

## 2.3. Steady state kinetic study

Oxidation of toluene was carried out in an atmospheric continuous plug flow reactor (Pyrex tube, i.d.  $1/2\text{ in.}$ ) located inside an oven (Binder, FP 115) to control the reaction temperature. Kinetic data were obtained at four different temperature levels of  $70$ ,  $80$ ,  $90$  and  $100^\circ\text{C}$  since catalyst deactivation occurs below  $70^\circ\text{C}$  [10]. Toluene was supplied from a mixture of toluene/nitrogen (Praxair, 300 ppm toluene, balance of nitrogen). Ozone was generated using an ozone generator (AZCO Industries LTD, HTU-500S) from pure oxygen (Praxair, 99.993%). The flow rates of toluene/nitrogen and ozone/oxygen streams were adjusted by two mass flow controllers (Brooks, SLA 5850) in order to achieve desired concentrations of toluene and ozone in the gas phase. The total flow rate of the reactants entering the reactor was  $1000\text{ ml/min}$  in all runs. The schematic of the experimental set-up is presented before [10]. Experiments were conducted with either constant toluene partial pressure of  $240 \times 10^{-6}\text{ atm}$  while ozone partial pressure was changed from  $1050$  to  $3000 \times 10^{-6}\text{ atm}$  or constant ozone partial pressure of  $1050 \times 10^{-6}\text{ atm}$  with toluene partial pressure in the range of  $90\text{--}240 \times 10^{-6}\text{ atm}$ . The space time of the reactor was between  $0$  and  $1212\text{ kg}_{\text{cat. mol}}^{-1}\text{ s}$ .  $\text{MnO}_x/\gamma$ -alumina (10%) was diluted with fine particles of silica carbide to prevent gas phase channeling and temperature gradients along the catalyst bed. Silica carbide was inert in the reaction. Toluene conversions were determined using GC-MS (Agilent, 7890-5975C) with a capillary column (Varian, Select Permanent Gasses/ $\text{CO}_2$ , CP7429). CO and  $\text{CO}_2$  were the most abundant reaction products in all temperature and pressure ranges. The uncertainty of the measured toluene conversions was estimated to be 1.5% in terms of standard error.

In order to check the effect of particle size on activity of the catalyst and to inhibit internal mass transfer limitation on the reaction rate, different ranges of catalyst particle sizes were tested for the reaction. The result is shown in Fig. S.2 of the Supplementary

document. It was observed that the activity of the catalyst,  $\text{MnO}_x/\gamma$ -alumina (10%), drops due to transport limitations when particles larger than 208  $\mu\text{m}$  were used. Thus, experiments were conducted using catalysts with particle size less than 208  $\mu\text{m}$ .

Plots of toluene conversion versus space time were used in order to obtain initial reaction rates of toluene oxidation ( $r_{\text{tol.}}$ ) based on the following equation:

$$r_{\text{tol.}} = \frac{dX_{\text{tol.}}}{d(W_{\text{cat.}}/F_{\text{tol.},\text{in}})} \quad (6)$$

in which,  $X_{\text{tol.}}$ ,  $W_{\text{cat.}}$  and  $F_{\text{tol.},\text{in}}$  represent toluene conversion, catalyst weight and inlet molar flow rate of toluene, respectively. Two numerical methods were used to estimate the initial reaction rates based on Eq. (6). The first method was based on fitting the conversion data by smoothing splines in MATLAB R2006a curve fitting toolbox and obtaining the initial reaction rates by differentiating the splines at zero space time. The second method was based on the fitting of the data with Eq. (7) and calculating the initial rates by product of A and B [29]:

$$X_{\text{tol.}} = A \left[ 1 - \exp \left[ -B \times \left( \frac{W_{\text{cat.}}}{F_{\text{tol.},\text{in}}} \right) \right] \right] \quad (7)$$

$A$  and  $B$  are the fitting parameters evaluated by fitting of Eq. (7) to conversion versus space time data. The initial rates calculated from the two methods, smoothing splines and Eq. (7), were averaged and used for kinetic analysis.

Kinetic models were fitted to the experimental data by nonlinear least squares technique in MATLAB R2006a using lsqnonlin function to minimize the sum of squares:

$$\text{minimize} \sum_i \sum_j (r_{\text{exp.},ij} - r_{\text{cal.},ij})^2 \quad (8)$$

$r_{\text{exp.}}$  and  $r_{\text{cal.}}$  denote experimental and calculated initial rates of toluene oxidation, respectively. Index  $i$  refers to different temperature levels (70, 80, 90 and 100 °C) and index  $j$  refers to  $j$ th reaction rate at temperature level  $i$ , corresponding to specific toluene and ozone partial pressures. In fact, model parameters including rate constants, toluene adsorption entropy, toluene adsorption enthalpy and activation energies were simultaneously estimated by Eq. (8) which allows non-isothermal fitting of the data. Toluene rate constant and toluene pressure adsorption equilibrium constant are defined by Eqs. (9) and (10), respectively:

$$k = k_0 \exp \left[ -\frac{E}{RT} \right] \quad (9)$$

$$K_{\text{tol.}} = \frac{K}{P^0} = \left( \frac{1}{P^0} \right) \times \exp \left[ \frac{\Delta S}{R} - \frac{\Delta H}{RT} \right] \quad (10)$$

$k$ ,  $k_0$  and  $K$  are toluene reaction rate constant, pre-exponential factor and dimensionless adsorption equilibrium constant, respectively.  $K_{\text{tol.}}$  is the toluene pressure equilibrium constant.  $\Delta S$  and  $\Delta H$  are entropy and enthalpy of adsorption of toluene.  $R$  is the universal gas constant and  $P^0$  is the pressure of standard state for gases which is 1 atm.

Kinetic models can be compared by  $F$ -test in order to evaluate the goodness of fits [30]:

$$F_c = \frac{\sum_i \sum_j (r_{\text{cal.},ij})^2}{\sum_i \sum_j (r_{\text{exp.},ij} - r_{\text{cal.},ij})^2 / DF} \quad (11)$$

Definitions of  $i$  and  $j$  indices are the same as Eq. (8).  $DF$  is the degrees of freedom defined as the difference between the number of experimental data points and the number of fitting parameters ( $p$ ). The best model among the available models can be distinguished by Eq. (11), suggesting that models with higher  $F_c$  values have higher regression significant.

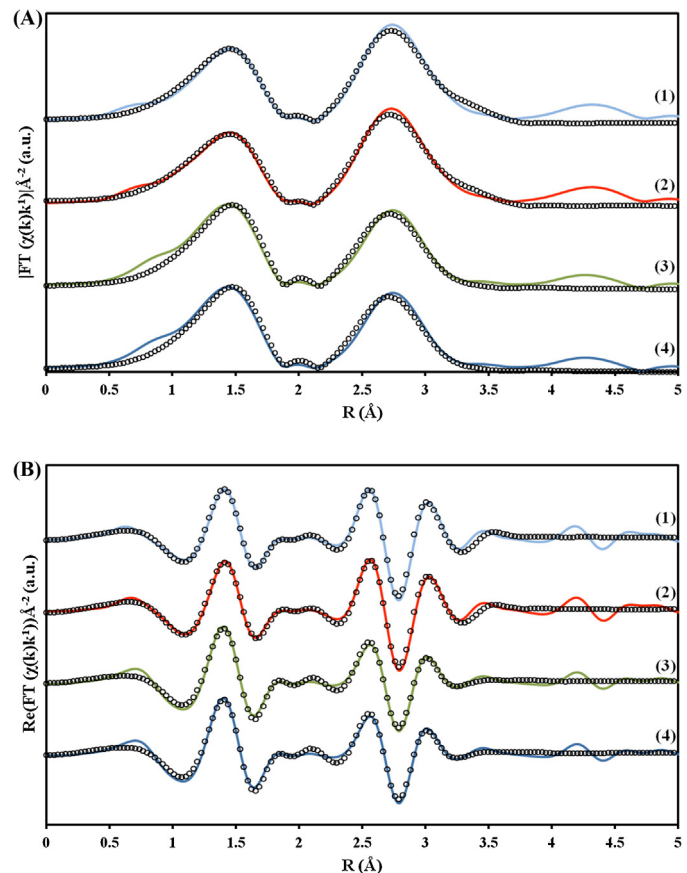


**Fig. 1.** (A) Magnitude and (B) real part of the Fourier transform (uncorrected phase shift) of Mn K-edge of the samples, solid lines are the data and symbols are the fitting; (1)  $\text{Mn}_2\text{O}_3$ , averaging method, (2)  $\text{Mn}_2\text{O}_3$ , Bond Valence Model, (3)  $\text{MnO}_x/\gamma$ -alumina (10%), averaging method, (4)  $\text{MnO}_x/\gamma$ -alumina (10%), Bond Valence Model.

### 3. Results and discussion

#### 3.1. EXAFS study

Mn K-edge EXAFS fitting of  $\text{Mn}_2\text{O}_3$  reference material and  $\text{MnO}_x/\gamma$ -alumina (10%), was carried out based on two methods. The first method is based on integrating the two Mn sites into one single site by averaging their coordination numbers based on their site occupancy which has been explained in detail before [10]. The second method is based on the Bond Valence Model which was described in Section 2.2. Magnitude and real part of the Fourier transform of the data and the fittings are shown in Fig. 1. Table 1 contains the parameters obtained for the fitting of the reference material and Table 2 summarizes the fitting result of the catalyst. It should be noted that CNs reported in Table 1 are fixed parameters obtained from crystallography data of  $\text{Mn}_2\text{O}_3$  while CNs in Table 2 are calculated from the EXAFS fitting of the catalyst.

Referring to Table 1, it can be seen that the averaging method results in an amplitude reduction factor ( $S_0^2$ ) of 0.83. This method locates the first shell oxygen atoms at ca. 1.88, 1.97 and 2.23 Å with CN of 1.5, 3 and 1.5, respectively. Two Mn atoms are also resolved at the second and third shells at ca. 3.11 and 3.62 Å, respectively. There are almost 17 independent points in the fitting range and 8 fitting parameters in the averaging method resulting in 9 degrees of freedom. On the other hand, the Bond Valence Model results in an amplitude reduction factor of 0.88 with roughly 17 independent points, 10 fitting variables and 7 degrees of freedom. There are 6 oxygen atoms at ca. 1.99 Å away from Mn atoms in the first Mn site (Mn1) whereas three sets of two oxygen atoms are located at ca.

**Table 1**EXAFS fitting result of the reference material ( $\text{Mn}_2\text{O}_3$ ).

$S_0^2 = 0.83 \pm 0.12, E_0 = 3.48 \pm 1.31, R_f = 1.9\%, \chi^2_\nu = 3416^{\text{a}}$ (Averaging method)				
Path		CN <sup>b</sup>	$\sigma^2 (\times 10^{-3} \text{ \AA}^2)$	$R (\text{ \AA})$
$\text{Mn}_2\text{O}_3$ (Averaging method)	Mn–O	1.5	$6.8 \pm 2.1$	$1.883 \pm 0.012$
	Mn–O	3	$6.8 \pm 2.1$	$1.969 \pm 0.012$
	Mn–O	1.5	$6.8 \pm 2.1$	$2.233 \pm 0.012$
	Mn–Mn	6	$7.7 \pm 1.5$	$3.113 \pm 0.011$
	Mn–Mn	6	$18.9 \pm 4.9$	$3.617 \pm 0.036$
$S_0^2 = 0.88 \pm 0.16, E_0 = 2.71 \pm 1.43, R_f = 1.7\%, \chi^2_\nu = 4573^{\text{a}}$ (Bond Valence Model)				
Mn1		Mn2		
Path	CN <sup>b</sup>	$\sigma^2 (\times 10^{-3} \text{ \AA}^2)$	$R (\text{ \AA})$	Path
$\text{Mn}_2\text{O}_3$ (Bond Valence Model)	Mn–O	6	$6.5 \pm 2.6$	$1.986 \pm 0.031$
	Mn–Mn	6	$8.3 \pm 1.9$	$3.110 \pm 0.012$
	Mn–Mn	6	$21.0 \pm 6.1$	$3.606 \pm 0.041$

<sup>a</sup> Correlations between the fitting parameters are less than 0.9.<sup>b</sup> Coordination numbers (CNs) are fixed from crystallography data.

1.87, 1.98 and 2.25 Å around the second Mn site (Mn2). The second Mn shell is found around the first and second Mn sites at ca. 3.11 and 3.12 Å, respectively with CN of 6. The third shell also has 6 Mn atoms which are located at ca. 3.61 and 3.62 Å from the first and second Mn sites, respectively.

By comparing the results of the two methods, it can be seen that the obtained parameters are very close to each other. For example,  $\sigma^2$  of the first shell of oxygen atoms obtained by the averaging method is  $6.8 \times 10^{-3} \text{ \AA}^2$  whereas this value from the Bond Valence Model is  $6.5 \times 10^{-3} \text{ \AA}^2$ . The same similarities can also be observed in  $\sigma^2$  of the Mn shells, the amplitude reduction factor (0.83 versus 0.88) and interatomic distances. The  $R_f$  (percentage of absolute misfit between the data and theory) of the averaging method and the Bond Valence Model are 1.9 and 1.7%, respectively. The reduced chi-square values of 3416 for the averaging method and 4573 for the Bond Valence Model are also close to each other, showing that the two methods have almost the same statistical significance.

The results of EXAFS studies reported in Table 1, are comparable with the EXAFS study of  $\text{Mn}_2\text{O}_3$  (bixbyite) performed by Longo et al. [16]. Basically, the authors have modeled the theoretical EXAFS signal of  $\text{Mn}_2\text{O}_3$  by considering 6 oxygen atoms at ca. 1.88 Å, 6 manganese atoms at ca. 3.12 Å and 6 manganese atoms at ca. 3.60 Å. They have fixed the oxygen and manganese coordination numbers along with a predetermined value of 0.74 for  $S_0^2$ . Their model has

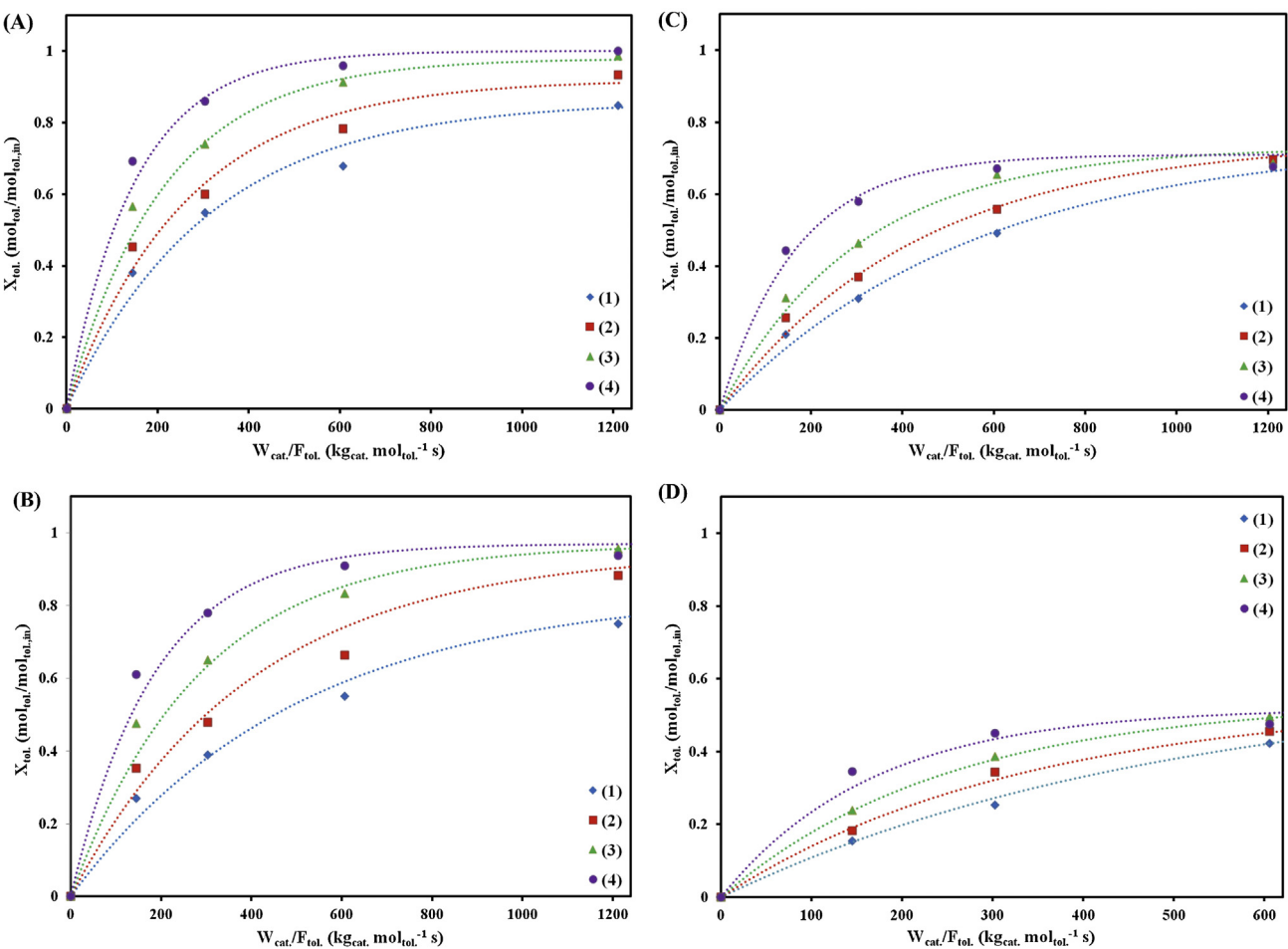
resulted in  $\sigma^2$  of  $7 \times 10^{-3} \text{ \AA}^2$  for the first oxygen shell which is very close to  $\sigma^2$  reported in this work for  $\text{Mn}_2\text{O}_3$  reference material, i.e.  $6.8 \times 10^{-3} \text{ \AA}^2$ .

Table 2 shows the results of the fitting of the catalyst,  $\text{MnO}_x/\gamma$ -alumina (10%), using the two methods. The amplitude reduction factors obtained from EXAFS fitting of the reference material were used as fixed parameters for the fitting of the catalyst by each method. This technique is generally used to untangle CN and  $S_0^2$  which are completely correlated to each other by product of CN.  $S_0^2$  in the EXAFS equation [28,31]. Using the averaging method, there were 5.5 oxygen atoms and 5.9 Mn atoms at the first and second Mn shells, respectively. 1.8, 2.3 and 1.4 oxygen atoms were found at ca. 1.89, 1.98 and 2.24 Å, respectively. The obtained CNs are close to oxygen and Mn coordination numbers at the first and second shells of  $\text{Mn}_2\text{O}_3$  which are 6 for each shell. Fitting of the catalyst were carried out with roughly 17 independent points, 9 fitting parameters and 8 degrees of freedom. It has to be noted that the results of the EXAFS fitting of the catalyst by the averaging method is slightly different from what has been reported previously since there are small changes in the fitting range and the amplitude reduction factor value [10]. On the other hand, the Bond Valence Model results in 5.4 oxygen atoms around the first Mn site (Mn1). These oxygen atoms are located at ca. 1.97 Å from Mn1 while three sets of oxygen atoms containing 1.8 oxygen atoms are found at ca. 1.88, 1.96 and 2.23 Å from the second Mn site (Mn2). 6.4 Mn atoms are

**Table 2**EXAFS fitting result of  $\text{MnO}_x/\gamma$ -alumina (10%).

$E_0 = 5.13 \pm 1.0, R_f = 1.5\%, \chi^2_\nu = 2485^{\text{a}}$ (Averaging method)				
Path		CN	$\sigma^2 (\times 10^{-3} \text{ \AA}^2)$	$R (\text{ \AA})$
$\text{MnO}_x/\gamma$ -alumina (10%) (Averaging method)	Mn–O	$1.8 \pm 0.7$	$4.6 \pm 1.6$	$1.894 \pm 0.028$
	Mn–O	$2.3 \pm 0.8$	$4.6 \pm 1.6$	$1.980 \pm 0.028$
	Mn–O	$1.4 \pm 0.6$	$4.6 \pm 1.6$	$2.244 \pm 0.028$
	Mn–Mn	$5.9 \pm 1.1$	$9.6 \pm 2.0$	$3.128 \pm 0.010$
$E_0 = 5.0 \pm 0.98, R_f = 1.7\%, \chi^2_\nu = 1573^{\text{a}}$ (Bond Valence Model)				
Mn1		Mn2		
Path	CN	$\sigma^2 (\times 10^{-3} \text{ \AA}^2)$	$R (\text{ \AA})$	Path
$\text{MnO}_x/\gamma$ -alumina (10%) (Bond Valence Model)	Mn–O	$5.4 \pm 0.7$	$4.3 \pm 2.4$	$1.971 \pm 0.038$
	Mn–Mn	$6.4 \pm 1.2$	$9.8 \pm 2.1$	$3.118 \pm 0.010$

<sup>a</sup> Correlations between the fitting parameters are less than 0.9.



**Fig. 2.** Toluene conversion versus space time at constant ozone partial pressure ( $P_{\text{o}_3}$ ) of  $1050 \times 10^{-6}$  atm and variable toluene partial pressures ( $P_{\text{tol}}$ ) at different temperatures; (A)  $P_{\text{tol}} = 90 \times 10^{-6}$  atm, (B)  $P_{\text{tol}} = 120 \times 10^{-6}$  atm, (C)  $P_{\text{tol}} = 180 \times 10^{-6}$  atm, (D)  $P_{\text{tol}} = 240 \times 10^{-6}$  atm; (1)  $70^\circ\text{C}$ , (2)  $80^\circ\text{C}$ , (3)  $90^\circ\text{C}$ , (4)  $100^\circ\text{C}$ , dotted lines show the trend of data.

estimated to be at the second shell of Mn1 and Mn2 with bond length of ca. 3.12 and 3.13 Å, respectively. The number of independent points, fitting parameters and degrees of freedom in the Bond Valence Model were the same as the averaging method used to model the catalyst. The estimated oxygen CNs and interatomic distances were put into Eqs. (4) and (5) to calculate the formal oxidation state of Mn1 and Mn2 sites. It was determined that oxidation states of Mn in Mn1 and Mn2 are 3.1 and 2.8, respectively which are very close to the formal oxidation state of Mn in the catalysts (+3), assuming that all manganese oxides are in  $\text{Mn}_2\text{O}_3$  phase.

Results of the fitting of the catalysts obtained by the averaging method and the Bond Valence Model are also similar. Oxygen and Mn interatomic bond lengths, coordination numbers and  $\sigma^2$  obtained from each method are very close. The  $R_f$  is 1.5 and 1.7% for the averaging method and the Bond Valence Model with reduced chi-squares of 2485 and 1573, respectively. This shows that the two methods have the same statistical significance and can be used for EXAFS analysis of  $\text{Mn}_2\text{O}_3$  containing catalysts. However, the Bond Valence Model can be considered as a more general approach for EXAFS fitting of complicated crystal structures such as  $\text{Mn}_2\text{O}_3$  since it does not impose any simplification on the unit cell structure. Nevertheless, the Bond Valence Model shows that the averaging method results in feasible and valid solutions and can be used to model EXAFS signal of oxides of manganese such as  $\text{Mn}_2\text{O}_3$  and  $\text{Mn}_3\text{O}_4$ .

### 3.2. Kinetic study

The effect of toluene and ozone partial pressures on toluene conversion at different reactor space times and temperatures is shown in Figs. 2 and 3. Fig. 2 indicates changes in toluene conversion at constant ozone partial pressure ( $P_{\text{o}_3}$ ) when toluene partial pressure ( $P_{\text{tol}}$ ) is increased. Toluene conversions ( $X_{\text{tol}}$ ) versus space time ( $W_{\text{cat}}/F_{\text{tol}}$ ) at each toluene partial pressure are shown in Fig. 2A–D. Results show that at a constant reactor space time, toluene conversion decreases with increase of toluene partial pressure while toluene conversions increase by increasing the temperature. Figs. 2D and 3A and B show the effect of  $P_{\text{o}_3}$  on toluene conversion when toluene partial pressure was kept constant at  $240 \times 10^{-6}$  atm. In contrast to the result of fixed  $P_{\text{o}_3}$ , toluene conversions increase by increasing  $P_{\text{o}_3}$  at a fixed reactor space time.

Initial reaction rates were estimated from Figs. 2 and 3 based on the methods explained in Section 2.3. The initial reaction rates versus toluene or ozone partial pressures at fixed ozone or toluene partial pressures are shown in Figs. 4 and 5. It can be observed in Fig. 4A that initial reaction rates decrease by increase of toluene partial pressure at constant ozone partial pressure, indicating the inhibitory effect of the toluene in this reaction. On the other hand, Fig. 4B shows that initial reaction rates increase by increase of ozone partial pressure at constant toluene partial pressure. Figs. 4 and 5 also contain predicated initial reaction rates obtained from two

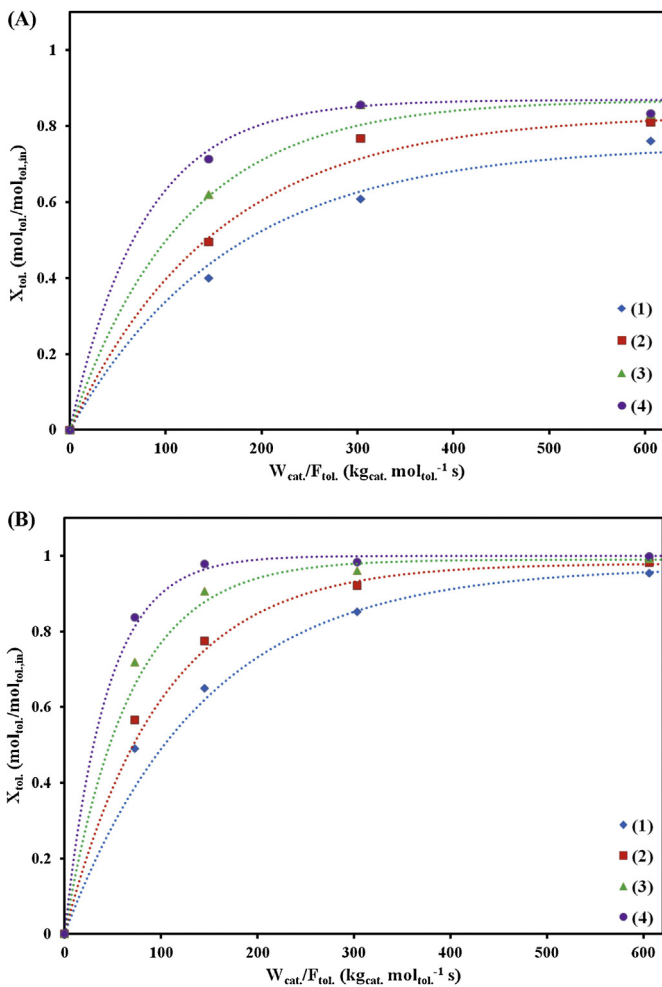


**Fig. 3.** Toluene conversion versus space time at constant toluene partial pressure ( $P_{\text{tol.}}$ ) of  $240 \times 10^{-6}$  atm and variable ozone partial pressures ( $P_{\text{ozone}}$ ) at different temperatures; (A)  $P_{\text{ozone}} = 2000 \times 10^{-6}$  atm, (B)  $P_{\text{ozone}} = 3000 \times 10^{-6}$  atm; (1)  $70^\circ\text{C}$ , (2)  $80^\circ\text{C}$ , (3)  $90^\circ\text{C}$ , (4)  $100^\circ\text{C}$ , dotted lines show the trend of data.

different kinetic models. The first model is a power law model (Fig. 4) and the second model is based on a Langmuir–Hinshelwood mechanism (Fig. 5) which was proposed originally for oxidation of acetone by ozone over silica supported manganese oxides [19]. The latter model was denoted by LH1.

The power law model is expressed as:

$$r_{\text{tol.}} = k P_{\text{tol.}}^n P_{\text{ozone}}^m \quad (12)$$

The result of fitting of Eq. (12) to the initial reaction rates is included in Table 3 and Fig. 4. The reaction orders with respect to toluene and ozone are  $-1$  and  $2$ , respectively. Fig. 4A indicates that  $P_{\text{tol.}}$  has a negative effect on the initial reaction rate causing the reaction rate to decrease by increase of toluene partial pressure. This results in reaction order of  $-1$  in Eq. (12) for toluene. On the other hand, Fig. 4B shows that initial rate of toluene oxidation increases by increase of ozone partial pressure, leading to

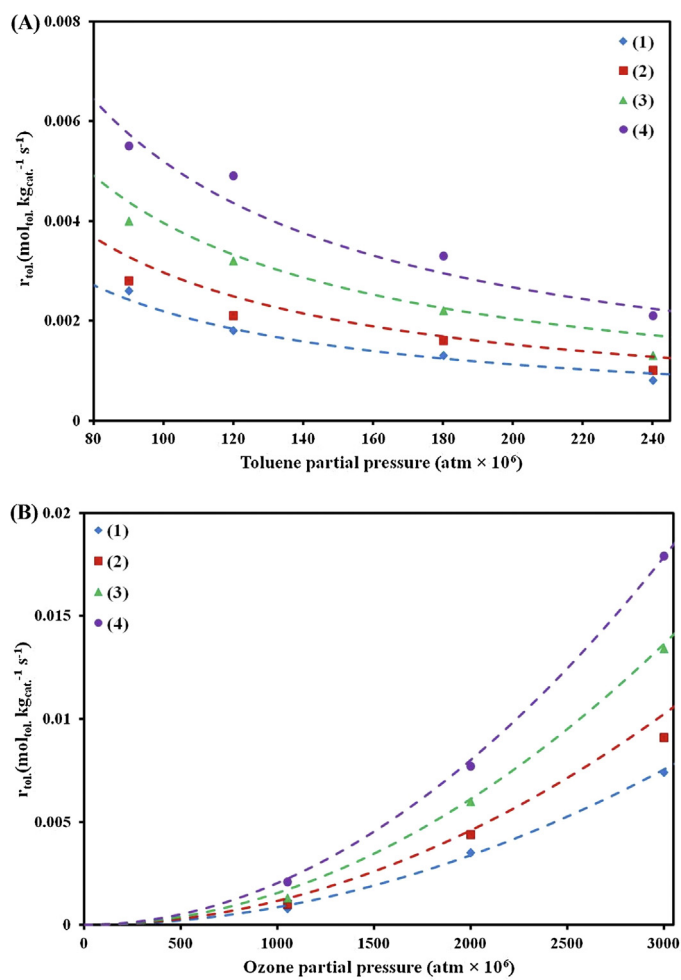


**Fig. 4.** Initial reaction rates and the power law model; (A) Constant ozone partial pressure ( $P_{\text{ozone}}$ ) at  $1050 \times 10^{-6}$  atm, (B) Constant toluene partial pressure ( $P_{\text{tol.}}$ ) at  $240 \times 10^{-6}$  atm; (1)  $70^\circ\text{C}$ , (2)  $80^\circ\text{C}$ , (3)  $90^\circ\text{C}$ , (4)  $100^\circ\text{C}$ , dashed lines show the predicted initial reaction rates by the power law model.

ozone reaction order of  $2$ . Apparent activation energy ( $E$ ) of the reaction is determined to be  $31 \text{ kJ mol}^{-1}$  which is close to the value reported by Naydenov and Mehandjiev for oxidation of benzene over  $\text{MnO}_2$  by ozone, i.e.  $30 \text{ kJ mol}^{-1}$  [32]. The apparent activation energy of the reaction ( $31 \text{ kJ mol}^{-1}$ ) is lower than the activation energy of catalytic total oxidation of toluene by oxygen which has been reported to be between  $75$  and  $106 \text{ kJ mol}^{-1}$  [33]. The decrease of the activation energy can be considered to be the main reason for the effectiveness of oxidation of VOCs by ozone which makes it possible to oxidize VOCs below  $100^\circ\text{C}$ . The activation energy of the reaction ( $31 \text{ kJ mol}^{-1}$ ) is also lower than the activation energy ( $55.6 \text{ kJ mol}^{-1}$ ) of homogeneous reaction between toluene and ozone reported for partial oxidation of toluene [34]. This indicates that the oxidation of toluene by ozone over  $\text{MnO}_x/\gamma\text{-alumina}$  is a heterogeneous reaction that occurs on manganese oxides.

As mentioned before, the second model is based on a Langmuir–Hinshelwood mechanism suggested for catalytic oxidation of acetone by ozone [19]. The elementary steps of this mechanism are shown in Table 4. The mechanism consists of two catalytic cycles. The first cycle is ozone decomposition cycle which is shown by steps (1) to (3). These three steps are considered for decomposition of ozone to atomic oxygen and peroxide species which eventually convert ozone to molecular oxygen. The second cycle is composed of quasi equilibrated adsorption of toluene in

**Table 3**  
Fitting results of the power law model.

$r_{\text{tol.}} = k P_{\text{tol.}}^n P_{\text{ozone}}^m, k = k_0 \exp\left(\frac{-E}{RT}\right)$				
$n$	$m$	$k_0 (\text{mol}_{\text{tol.}} \text{ kg}_{\text{cat.}}^{-1} \text{ s}^{-1} \text{ atm}^{-1})$	$E (\text{kJ mol}^{-1})$	$F_c$
$-1$	$2$	$1 \times 10^4$	$31$	$1705$

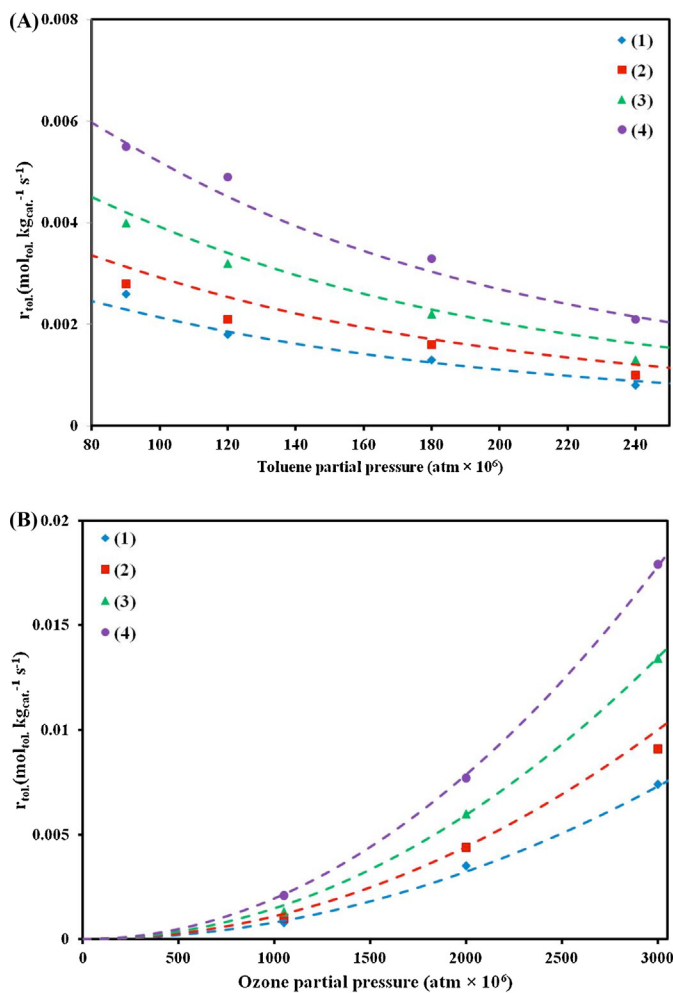


**Fig. 5.** Initial reaction rates and the LH1 mechanism; (A) Constant ozone partial pressure ( $P_{\text{o}_3}$ ) at  $1050 \times 10^{-6}$  atm, (B) Constant toluene partial pressure ( $P_{\text{tol}}$ ) at  $240 \times 10^{-6}$  atm; (1)  $70^\circ\text{C}$ , (2)  $80^\circ\text{C}$ , (3)  $90^\circ\text{C}$ , (4)  $100^\circ\text{C}$ , dashed lines show the predicted initial reaction rates by the LH1 mechanism.

step (4) and reaction with atomic oxygen in step (5) to activate the adsorbed toluene molecule and start the oxidation reaction. It is assumed that further steps after step (5) are fast and are not significant from kinetic point of view. The two cycles are coupled to each other by consumption of atomic oxygen. If  $n$  oxygen

atoms are consumed in step (5), the rate of toluene oxidation will be:

$$r_{\text{tol}} = K_{\text{tol}} \frac{k'_1 P_{\text{tol}} P_{\text{o}_3}^n}{(1 + k'_2 P_{\text{o}_3} + K_{\text{tol}} P_{\text{tol}})^{n+1}} \quad (13)$$

The derivation of Eq. (13) is given in [19]. The definition of parameters used in Eq. (13) is provided in Table 4. The first term in the denominator of Eq. (13) corresponds to the fraction of vacant catalyst active sites ( $\theta^*$ ) which are assumed to be Mn atoms. The second term in the denominator ( $k'_2 P_{\text{o}_3}$ ) is related to the fraction of active sites covered by peroxide species ( $\theta_{\text{O}_2^*}$ ) and the last term ( $K_{\text{tol}} P_{\text{tol}}$ ) represents the fraction of active sites covered by toluene molecules ( $\theta_{\text{tol}}^*$ ). Concentration of surface atomic oxygen is assumed to be negligible due to high reactivity and short lifetime of these species. Authors have shown that peroxide species are spectators in catalytic oxidation of acetone by ozone and atomic oxygen is responsible for the oxidation reaction [19]. However, they have considered the peroxide species in the calculation of the fraction of active sites.

Results of the fitting of Eq. (13) to the initial reaction rates are shown in Table 4 and Fig. 5. It was found that 2 oxygen atoms are required to start the oxidation reaction by step (5). The first pre-exponential factor ( $k'_{10}$ ) is much larger than the second pre-exponential factor ( $k'_{20}$ ). The low value of  $k'_{20}$  suggests that the concentration of peroxide species is low on the surface of the catalyst and they can be neglected compared to the fraction of active sites covered by toluene. Therefore, the fraction of surface peroxide ( $\theta_{\text{O}_2^*}$ ) can be excluded from the kinetic model because of the low value of  $k'_{20}$  compared to the pressure equilibrium constant of toluene adsorption ( $K_{\text{tol}}$ ). The high value of  $k'_{10}$  shows that the step (5) is probably a fast step with high reaction rate constant since  $k'_1$  is defined as the product of  $k_5$  and  $k'_2$ . The value of  $E'_2$  ( $89 \text{ kJ mol}^{-1}$ ) is positive and shows that activation energy of desorption of oxygen molecule in step (3) is larger than the activation energy of ozone adsorption in step (1). This is in agreement with the difference ( $60 \text{ kJ mol}^{-1}$ ) between adsorption and desorption activation energies at zero surface coverage reported for decomposition of ozone by manganese oxides supported on alumina [35]. The activation energy of step (5) can also be estimated by subtraction of  $E'_1$  from  $E'_2$  which results in an activation energy of  $48 \text{ kJ mol}^{-1}$  for the step (5) in Table 1. The value of entropy ( $\Delta S_{\text{tol}}$ ) and enthalpy ( $\Delta H_{\text{tol}}$ ) of toluene adsorption turned out to be positive, suggesting an endothermic toluene adsorption. The endothermic adsorption is not very common and cannot be easily justified as the entropy of the toluene molecule increases after adsorption. Similar results have been reported for catalytic ozonation of acetone by ozone and catalytic oxidation of benzene by oxygen, in which positive values were reported for  $\Delta H_{\text{tol}}$  and  $\Delta S_{\text{tol}}$  [19,36]. Nevertheless,

**Table 4**

Elementary steps of the LH1 mechanism and the fitting results.

Elementary steps based on [19]	Reaction rate/equilibrium constant					
(1) $\text{O}_3 + * \rightarrow \text{O}_2 + \text{O}^*$	$k_1$					
(2) $\text{O}_3 + \text{O}^* \rightarrow \text{O}_2 + \text{O}_2^*$	$k_2$					
(3) $\text{O}_2^* \rightarrow \text{O}_2 + *$	$k_3$					
(4) $\text{C}_6\text{H}_5-\text{CH}_3 + * \rightleftharpoons \text{C}_6\text{H}_5-\text{CH}_3^*$	$K_{\text{tol}}$					
(5) $\text{C}_6\text{H}_5-\text{CH}_3^* + n\text{O}^* \rightarrow \text{products}$	$k_5$					
$r_{\text{tol}} = K_{\text{tol}} \frac{k'_1 P_{\text{tol}} P_{\text{o}_3}^n}{(1 + k'_2 P_{\text{o}_3} + K_{\text{tol}} P_{\text{tol}})^{n+1}}, k'_1 = \frac{k_1 k_5}{k_3} = k'_{10} \exp\left(\frac{-E'_1}{RT}\right), k'_2 = \frac{k_1}{k_3} = k'_{20} \exp\left(\frac{-E'_2}{RT}\right), K_{\text{tol}} = \frac{\exp((\Delta S_{\text{tol}}/R) - (\Delta H_{\text{tol}}/RT))}{P_{\text{o}_3}}$						
$n$	$k'_{10} (\text{mol}_{\text{tol}} \text{ kg}_{\text{cat}}^{-1} \text{ s}^{-1} \text{ atm}^{-2})$	$E'_1 (\text{kJ mol}^{-1})$	$k'_{20} (\text{atm}^{-1})$	$E'_2 (\text{kJ mol}^{-1})$	$\Delta S_{\text{tol}} (\text{J mol}^{-1} \text{ K}^{-1})$	$\Delta H_{\text{tol}} (\text{kJ mol}^{-1})$
2	$3 \times 10^{10}$	41	0.2	89	100	8
Temperature ( $^\circ\text{C}$ )		70	80	90	100	$F_c$
$K_{\text{tol}} (\text{atm}^{-1})$	10,650	11,520	12,407	13,308	1001	

<sup>a</sup>  $\text{O}_3$  and  $\text{C}_6\text{H}_5-\text{CH}_3$  are the catalyst active site (Mn), ozone and toluene, respectively.

<sup>b</sup>  $P^0$  is pressure of standard state for gases, i.e. 1 atm.

Gibbs free energy change of the adsorption step is negative, indicating consistent thermodynamics. Apparent activation energy can be calculated by the following equation [37]:

$$E_{\text{cal.}}^{\text{app.}} = RT^2 \left( \frac{\partial \ln r}{\partial T} \right)_p \quad (14)$$

Inserting Eq. (13) into Eq. (14) with  $n$  equal to 2, results in:

$$E_{\text{cal.}}^{\text{app.}} = \Delta H_{\text{tol.}} + E'_1 - 3(E'_2 \theta_{O_2^*} + \Delta H_{\text{tol.}} \theta_{\text{tol.}*}) \quad (15)$$

$\theta_{O_2^*}$  is negligible in Eq. (15) due to the low value of  $k_2'$  and  $\theta_{\text{tol.}*}$  can be averaged over all pressure and temperature ranges. Considering an average value of 0.7 for  $\theta_{\text{tol.}*}$ , the apparent activation energy of the reaction ( $E_{\text{cal.}}^{\text{app.}}$ ) based on Eq. (13) is determined to be 33 kJ/mol which is close to the value obtained by the power law model. The  $F_c$  of the fittings based on the power law model and the LH1 mechanism are presented in Tables 3 and 4. It can be observed that the  $F_c$  corresponding to the power law model is larger than that of the LH1 mechanism since the number of fitting parameters is less in the power law model. However, both models perfectly represent the pattern of the experimental observations.

Even though the LH1 mechanism agrees well with the experimental data, it is not easy to justify the positive values of entropy and enthalpy of toluene adsorption. Thus, it was attempted to improve the LH1 mechanism based on evidence reported on mechanism of catalytic oxidation of hydrocarbons and especially toluene by atomic oxygen. It has been proposed that toluene interacts dissociatively with the surface of transition metal oxides via abstraction of one H atom from the methyl group producing one adsorbed proton and adsorbed radical benzyl species [38–40]. This step is considered to be the first step in oxidation of toluene. Chin et al. and G.-Dieguez et al. also proved with isotopic exchange experiments and density functional theory (DFT) calculations that C–H bond cleavage is the kinetically relevant step in oxidation of alkanes ( $C_nH_{2n+2}$ ) which occurs on catalyst active site pairs [41,42]. Menon et al. have also studied the reaction network of catalytic toluene oxidation by temporal analysis of products (TAP) and isotopic techniques [43]. They have observed that hydrogen abstraction from the methyl and phenyl groups occurs before oxidation of carbon atoms, resulting in release of  $H_2O$  before detection of  $CO_2$ . The application of C–H bond cleavage model for catalytic oxidation of hydrocarbons by ozone has also been used by Li and Oyama for catalytic ozonation of ethanol, even though the authors did not propose a rate equation based on this mechanism [2].

Therefore, a second Langmuir–Hinshelwood mechanism (LH2) is proposed for oxidation of toluene by ozone based on the initiation of the reaction by hydrogen abstraction from the methyl group of toluene [19,42,43]. The scheme of this mechanism is shown in Table 5. No by-products other than CO,  $CO_2$  and water were considered in the scheme. The first three steps in Table 5 are considered for decomposition of ozone. The fourth step is quasi equilibrated adsorption of toluene on the first active site. The fifth step is release of one proton on the second active site from the adsorbed toluene molecule to produce  $C_6H_5-CH_2^*$  and  $H^*$ .  $C_6H_5-CH_2^*$  undergoes successive H abstractions to produce more  $H^*$  and a hydrogen free carbon structure ( $C_6-C^*$ ) shown in step 6. The protons react with adsorbed oxygen atoms to produce  $OH^*$  in the seventh step. The produced  $OH^*$  species combine and produce water through steps 8 and 9. The next step would be the reaction of the carbon atom from the methyl group in step 10 to produce an adsorbed CO molecule leaving the  $C_6$  ring ( $C_6^*$ ). The ring opening occurs in step (11) of Table 5, in which adsorbed CO molecules are formed. The adsorbed CO molecules can be oxidized to  $CO_2$  in step (12) or desorb via step (13). The generated  $CO_2$  molecules can leave the surface in step (14). It has to be noted that step (6) and (11) are not elementary steps. Step (6) represents successive abstraction of hydrogen from

**Table 5**

Scheme of the Langmuir–Hinshelwood mechanism (LH2) based on C–H activation.

Step	Reaction rate/equilibrium constant
(1) $O_3 + ^* \rightarrow O_2 + O^*$	$k_1$
(2) $O_3 + O^* \rightarrow O_2 + O_2^*$	$k_2$
(3) $O_2^* \rightarrow O_2 + ^*$	$k_3$
(4) $C_6H_5-CH_3 + ^* \rightleftharpoons C_6H_5-CH_3^*$	$K_{\text{tol.}}$
(5) $C_6H_5-CH_3^* + ^* \rightarrow C_6H_5-CH_2^* + H^*$	$k_5$
(6) $C_6H_5-CH_2^* + 7^* \rightarrow C_6-C^* + 7H^*$	$k_6$
(7) $H^* + O^* \rightleftharpoons OH^* + ^*$	$K_7$
(8) $2OH^* \rightleftharpoons H_2O^* + O^*$	$K_8$
(9) $H_2O^* \rightleftharpoons H_2O + ^*$	$K_9$
(10) $C_6-C^* + O^* \rightarrow C_6^* + CO^*$	$k_{10}$
(11) $C_6^* + 6O^* \rightarrow 6CO^*$	$k_{11}$
(12) $CO^* + O^* \rightarrow CO_2^* + ^*$	$k_{12}$
(13) $CO_2^* \rightleftharpoons CO + ^*$	$K_{13}$
(14) $CO \rightleftharpoons CO_2 + ^*$	$K_{14}$

$C_6H_5-CH_2^*$  while step (11) indicates successive oxidation of carbon atoms in the  $C_6$  ring by atomic oxygen.

If we assume that all  $O^*$  atoms generated in step (1) are consumed for oxidation of toluene and there are no by-products other than CO,  $CO_2$  and water, steady state site balance for  $O^*$  results in:

$$r_1 = k_1 P_{O_3} \theta^* = v_{O_3} r_5 = v_{O_3} k_5 K_{\text{tol.}} \theta^{*2} \quad (16)$$

The detail of the derivation of Eq. (16) is provided in section 3 of the Supplementary document.  $v_{O_3}$  is theoretical stoichiometric coefficient of the reaction for ozone. Eq. (16) can be used to determine  $\theta^*$ :

$$\theta^* = \frac{k_1 P_{O_3}}{v_{O_3} k_5 K_{\text{tol.}} P_{\text{tol.}}} \quad (17)$$

Upon substitution of Eq. (17) into Eq. (16), rate of toluene oxidation becomes:

$$r_{\text{tol.}} = r_5 = \frac{r_1}{v_{O_3}} = \frac{k_1^2 P_{O_3}^2}{v_{O_3}^2 k_5 K_{\text{tol.}} P_{\text{tol.}}} = k_{\text{eff.}} P_{\text{tol.}}^{-1} P_{O_3}^2 \quad (18)$$

$$k_{\text{eff.}} = \frac{k_1^2}{v_{O_3}^2 k_5 K_{\text{tol.}}} \quad (19)$$

Eq. (18) is the rate equation of the LH2 mechanism showing that order of the reaction is –1 and 2 with respect to toluene and ozone, respectively. The rate equation of the LH2 model is the same as the rate expression obtained by the power law model via Eq. (12). Both models result in the same reaction orders for toluene and ozone. Therefore, one can estimate  $k_{\text{eff.}}$  from the value of pre-exponential factor ( $k_0$ ) and the activation energy ( $E$ ) reported in Table 3 for the power law model. Eq. (18) also shows that rate of toluene oxidation is proportional to the square of  $k_1$ , indicating that higher rates of ozone decomposition accelerate the rate of toluene oxidation.

In summary, two Langmuir–Hinshelwood mechanisms have been tested to explore the mechanism of catalytic oxidation of toluene by ozone. The LH1 mechanism has a deficiency due to predicting positive values for entropy and enthalpy of toluene adsorption which are not common in catalytic reactions [30,44]. The LH2 model explains the oxidation mechanism in more detail by considering the C–H bond cleavage from the methyl group. This step can be considered to be the kinetically relevant step in the oxidation of toluene. The LH2 model results in the same reaction orders obtained from the experimental data using the power law model. Further evaluation of the LH2 mechanism is possible by tracking the reaction rates at toluene partial pressures close to zero while ozone partial pressure is kept constant. One can show that the LH2 model is superior to the LH1 model by observing increase of toluene oxidation rate when toluene partial pressure approaches

zero. However, studying the reaction rates at lower toluene partial pressures is beyond the scope of this paper and can be explored in the future.

#### 4. Conclusion

The Bond Valence Model was used to fit the EXAFS signal of  $\text{Mn}_2\text{O}_3$  materials, consisting of two Mn sites with closely located oxygen atoms around each Mn site. The Bond Valence Model adds restraints to the EXAFS theoretical model in order to keep the formal oxidation state of Mn atoms close to +3. Results of the EXAFS fitting show that by considering the Bond Valence Model in the EXAFS fitting, it is possible to accurately distinguish the first shell oxygen atoms in each Mn site. It was also found that the result of the EXFAS study of  $\text{Mn}_2\text{O}_3$  based on averaging the two Mn sites into a single site is consistent with the result of the Bond Valence Model, confirming the validity of the averaging method.

Kinetic study of toluene oxidation over  $\text{MnO}_x/\gamma$ -alumina (10%) was performed by considering three different models to explain the initial reaction rates. The first model was based on the power law model which results in a low apparent activation energy, showing the heterogeneous nature of the reaction between ozone and toluene. It was also observed that toluene has inhibitory effect on the reaction rate while increase of ozone partial pressure favors the rate of toluene oxidation. The second model was a Langmuir–Hinshelwood mechanism proposed originally for catalytic oxidation of acetone by ozone. Result of the second model was consistent with the trend of the reactions rates, even though it led to an endothermic toluene adsorption. The third model was also a Langmuir–Hinshelwood type of mechanism which was developed based on toluene activation by abstraction of hydrogen from the methyl group of toluene. The C–H bond cleavage was assumed to be the relevant kinetic step in the oxidation of toluene. It was shown that the third model is identical to the power law model, resulting in the same reaction orders as determined by the power law model from the experimental data. Further studies are needed to validate the LH2 model over wider range of toluene partial pressure. It is also interesting to study the LH2 mechanism by isotopic exchange techniques, density functional theory (DFT) calculations and in-situ spectroscopy to provide more evidence about the elementary steps involved in the LH2 mechanism.

#### Acknowledgments

Financial support for this research work was provided by University of Saskatchewan and the Natural Sciences and Engineering Research Council of Canada (NSERC). XAS experiments were performed at the Canadian Light Source (CLS), which is supported by the NSERC, the National Research Council Canada, the Canadian Institutes of Health Research, the Province of Saskatchewan and Western Economic Diversification Canada. We are also grateful to Dr Ning Chen, beamline scientist at HXMA beamline, and Ms Jinru Lin for their help to run the samples.

#### Appendix A. Supplementary data

Supplementary material related to this article can be found, in the online version, at <http://dx.doi.org/10.1016/j.apcatb.2013.10.041>.

#### References

- [1] S.T. Oyama, Catal. Rev. Sci. Eng. 42 (2000) 279–322.
- [2] W. Li, S. Ted Oyama, Stud. Surf. Sci. Catal. (1997) 873–882 (Elsevier).
- [3] M. Stoyanova, P. Konova, P. Nikolov, A. Naydenov, S. Christoskova, D. Mehandjiev, Chem. Eng. J. 122 (2006) 41–46.
- [4] Y. Xi, C. Reed, Y.-K. Lee, S.T. Oyama, J. Phys. Chem. B 109 (2005) 17587–17596.
- [5] H. Einaga, S. Futamura, Appl. Catal. B 60 (2005) 49–55.
- [6] H. Einaga, Y. Teraoka, A. Ogata, Catal. Today 164 (2011) 571–574.
- [7] H.C. Wang, H.S. Liang, M.B. Chang, Chemosphere 82 (2011) 1090–1095.
- [8] H.C. Wang, H.S. Liang, M.B. Chang, J. Hazard. Mater. 186 (2011) 1781–1787.
- [9] M. Li, K.N. Hui, K.S. Hui, S.K. Lee, Y.R. Cho, H. Lee, W. Zhou, S. Cho, C.Y.H. Chao, Y. Li, Appl. Catal. B 107 (2011) 245–252.
- [10] E. Rezaei, J. Soltan, N. Chen, Appl. Catal. B 136–137 (2013) 239–247.
- [11] D. Zhao, C. Shi, X. Li, A. Zhu, B.W.-L. Jang, J. Hazard. Mater. 239–240 (2012) 362–369.
- [12] B. Dhandapani, S.T. Oyama, Appl. Catal. B 11 (1997) 129–166.
- [13] C. Reed, Y.-K. Lee, S.T. Oyama, J. Phys. Chem. B 110 (2006) 4207–4216.
- [14] H. Einaga, M. Harada, A. Ogata, Catal. Lett. 129 (2009) 422–427.
- [15] H. Einaga, Y. Teraoka, A. Ogata, J. Catal. 305 (2013) 227–237.
- [16] A. Longo, F.L. Liotta, G. Di Carlo, F. Giannici, A.M. Venezia, A. Martorana, Chem. Mater. 22 (2010) 3952–3960.
- [17] A.K.S.K. Sinha, M. Takahara, H. Azuma, T. Nonaka, N. Suzuki, N. Takahashi, J. Phys. Chem. C 112 (2008) 16028–16035.
- [18] A.K.S.K. Sinha, M. Takahara, H. Azuma, T. Nonaka, K. Fukumoto, Angew. Chem. Int. Ed. 46 (2007) 2891–2894.
- [19] C. Reed, Y. Xi, S.T. Oyama, J. Catal. 235 (2005) 378–392.
- [20] E. Rezaei, J. Soltan, Chem. Eng. J. 198–199 (2012) 482–490.
- [21] E. Rezaei, J. Soltan, N. Chen, J. Lin, Chem. Eng. J. 214 (2013) 219–228.
- [22] D.T. Jiang, N. Chen, W. Sheng, AIP Conf. Proc. 879 (2007) 800–803.
- [23] B. Ravel, M. Newville, J. Synchrotron Radiat. 12 (2005) 537–541.
- [24] J.J. Rehr, R.C. Alber, Rev. Mod. Phys. 72 (2000) 621–654.
- [25] M. Newville, J. Synchrotron Radiat. 8 (2001) 322–324.
- [26] M. Newville, Phys. Scr. T115 (2005) 159–161.
- [27] I.D. Brown, D. Altermatt, Acta. Cryst. B41 (1985) 244–247.
- [28] B. Ravel, EXAFS Analysis with FEFF and FEFFIT, Part 2: Commentary, 2001.
- [29] M.P. Heynderickx, J.W. Thybaut, H. Poelman, D. Poelman, G.B. Marin, Appl. Catal. B 95 (2010) 26–38.
- [30] G.F. Froment, K.B. Bischoff, J. De Wilde, Chemical Reactor Analysis and design, 3rd ed., John Wiley & Sons, Inc., United States of America, 2011.
- [31] S.D. Kelly, D. Hesterberg, B. Ravel, Analysis of soils and minerals using X-ray absorption spectroscopy, in: in: Methods of soil analysis, Part 5 –Mineralogical methods, Soil Science Society of America, Inc, Madison, WI, USA, 2008, pp. 387–463.
- [32] A. Naydenov, D. Mehandjiev, Appl. Catal. A 97 (1993) 17–22.
- [33] J. Bedia, J.M. Rosas, J. Rodríguez-Mirasol, T. Cordero, Appl. Catal. B 94 (2010) 8–18.
- [34] S. Toby, L.J. Van de Burgt, F.S. Toby, J. Phys. Chem. 89 (1985) 1982–1986.
- [35] R. Radhakrishnan, S.T. Oyama, J. Catal. 199 (2001) 282–290.
- [36] J.A. Barnard, D.S. Mitchell, J. Catal. 12 (1968) 386–397.
- [37] P.M. Heynderickx, J.W. Thybaut, H. Poelman, D. Poelman, G.B. Marin, J. Catal. 272 (2010) 109–120.
- [38] S.I.T. Andersson, J. Catal. 98 (1986) 138–149.
- [39] G. Busca, F. Cavani, F. Trifirò, J. Catal. 106 (1987) 471–482.
- [40] B. Irigoyen, A. Juan, S. Larrondo, N. Amadeo, Surf. Sci. 523 (2003) 252–266.
- [41] Y.-H. Chin, C. Buda, M. Neurock, E. Iglesia, J. Am. Chem. Soc. 133 (2011) 15958–15978.
- [42] M. García-Díéguez, Y.-H. Chin, E. Iglesia, J. Catal. 285 (2012) 260–272.
- [43] U. Menon, V.V. Galvita, G.B. Marin, J. Catal. 283 (2011) 1–9.
- [44] M.A. Vannice, Kinetics of Catalytic Reactions, 1st ed., Springer, United States of America, 2005.